CFD calculations on the unsteady aerodynamic characteristics of a tilt-rotor in a conversion mode

Li Peng, Zhao Qijun *, Zhu Qiuxian

National Key Laboratory of Science and Technology on Rotorcraft Aeromechanics, Nanjing University of Aeronautics and Astronautics, Nanjing 210016, China

Abstract   In order to calculate the unsteady aerodynamic characteristics of a tilt-rotor in a conversion mode, a virtual blade model (VBM) and an real blade model (RBM) are established respectively. A new multi-layer moving-embedded grid technique is proposed to reduce the numerical dissipation of the tilt-rotor wake in a conversion mode. In this method, a grid system generated abound the rotor accounts for rigid blade motions, and a new searching scheme named adaptive inverse map (AIM) is established to search corresponding donor elements in the present moving-embedded grid system to translate information among the different computational zones. A dual-time method is employed to fulfill unsteady calculations on the flowfield of the tilt-rotor, and a second-order centered difference scheme considering artificial viscosity is used to calculate the flux. In order to improve the computing efficiency, the single program multiple data (SPMD) model parallel acceleration technology is adopted, according to the characteristic of the current grid system. The lift and drag coefficients of an NACA0012 airfoil, the dynamic pressure distributions below a typical rotor plane, and the sectional pressure distributions on a three-bladed Branum–Tung tilt-rotor in hover flight are calculated respectively, and the present VBM and RBM are validated by comparing the calculated results with available experimental data. Then, unsteady aerodynamic forces and flowfields of an XV-15 tilt-rotor in different modes, such as a fixed conversion mode at different tilt angles (15°, 30°, 60°) and a whole conversion mode which converses from 0° to 90°, are numerically simulated by the VBM and RBM respectively. By analyses and comparisons on the simulated results of unsteady aerodynamic forces of the tilt-rotor in different modes, some meaningful conclusions about distorted blade-tip vortex distribution and unsteady aerodynamic force variation in a conversion mode are obtained, and these investigation results could provide a good foundation for tilt-rotor aircraft design in the future.

* Corresponding author. Tel.: +86 25 84893753.
  E-mail addresses: lp1987@nuaa.edu.cn (P. Li), zhaoqijun@nuaa.edu.cn (Q. Zhao), zhuqiuxian@nuaa.edu.cn (Q. Zhu).

1. Introduction

A tilt-rotor aircraft combines the advantages of vertical taking-off and landing capabilities of helicopters with higher forward speed and larger range of turboprop airplanes. Such characteristics enable the tilt-rotor aircraft to provide high-speed,

long-range flights coupled with runway independent operations, thus having a significant potential to improve the transport capacity and efficiency of the rotorcraft. The developments and requirements of the rotorcraft are introduced in Refs.[1,2]

The conversion process is one of the unique features of this rotorcraft. During this process, rotor control authority is mechanically phased out with the nacelle angle as the transition occurs from the rotor lift to wing lift mode, which would result in more severe wake distortion and unsteady blade loads. Research on tilt-rotor aircraft in a conversion mode is still a challenging problem, although extensive investigations on this rotorcraft in hover and cruise modes have been conducted during the past several decades, which can be found in Refs.[3–13] In contrast to time-consuming experimental investigations, the CFD method has become an important tool to analyze the aerodynamic force of a tilt-rotor in industrial practices. For example, Wissink et al.[14] employed a coupled unstructured-adaptive CFD approach to predict the aerodynamic performance of a tilt-rotor aeroacoustic model (TRAM) isolated tilt-rotor in a hover mode, and showed that this approach was able to obtain the figure of merit of the tilt-rotor effectively. Potsdam and Strawn[15] computed the performance of an isolated rotor in a steady state, and results agreed well with experimental data, which provided a wealth of flowfield details that could be used to analyze and improve the aerodynamic performance of the isolated tilt-rotor. Sheng and Narramore[16] applied a Navier–Stokes CFD method to analyze the aerodynamic characteristics of a quad tilt-rotor in an airplane mode and a fixed-conversion mode at a 75° nacelle tilt angle. Good agreements between the calculated results and experimental data have also been achieved.

However, most of their researches on tilt-rotors were concentrated in a hover or cruise mode, and limited applications were conducted in a conversion mode. During the tilt-rotor conversion process, it is challenging to calculate the unsteady flowfield and aerodynamic force of a tilt-rotor due to complicated blade motions and distorted blade-tip vortices. At the same time, the CFD method requires large computation consumption and an unsteady time stepping scheme should be considered carefully. To supplement these, a preliminary investigation is carried out to analyze such unsteady complex flows in this paper. Considering the complexity of the unsteady aerodynamic force of a tilt-rotor in a conversion mode, a virtual blade model (VBM) and an real blade model (RBM) are proposed and used to simulate the unsteady flowfield respectively. Firstly, the tilt-rotor is simulated simply by an actuator disk model in the VBM, aiming at providing fast and effective results. Then, a new highly-efficient multi-layer grid technique is put forward and established in the RBM to obtain detailed information about the unsteady flowfield with a considerable cost. In the methods, three-dimensional unsteady Navier–Stokes equations are discretized by Jameson's second-order cell-centered finite volume scheme and an implicit lower–upper symmetric Gauss–Seidel (LU-SGS) scheme. Finally, based on the methods above, the unsteady aerodynamic forces of the tilt-rotor in different conversion modes are calculated, and some meaningful conclusions are obtained.

2. Moving-embedded grid system

2.1. Coordinate systems definition

Based on the grid method for a conventional rotor developed by the corresponding author of this paper,[17,18] for a tilt-rotor

in a conversion mode, the rigid blade flapping, pitching, rotational motion, and tilting and translational motions are described as follows

$$\begin{cases} \theta(t) = \theta_0 - \theta_{1c} \cos \psi(t) - \theta_{1s} \sin \psi(t) \\ \beta(t) = A_0 - A_1 \cos \psi(t) - B_1 \sin \psi(t) \\ \psi(t) = \Omega t, \phi(t) = \Omega_{\text{tilt}} t \end{cases} \quad (1)$$

where θ_0 is the collective pitch angle, A_0 the coning angle, θ_{1c} and θ_{1s} represent the cyclic flapping coefficients, A_1 and B_1 represent the cyclic pitch coefficients, Ω is the rotor rotational speed, Ω_{tilt} the rotor conversion speed, t the time, ψ the azimuthal angle, ϕ the tilt angle.

At any physical time, the position of a typical point on the tilt-rotor blade $L_B(x, y, z, t)$ or among the transitional grid $L_T(x, y, z, t)$ system can be related to its initial position through the transformation of the coordinate system, which is given as follows

$$\begin{cases} L_B = R_{\phi(t)} R_{\psi(t)} R_{\beta(t)} R_{\theta(t)} L_B^0 = T_B L_B^0 \\ L_T = R_{\phi(t)} L_T^0 = T_T L_T^0 \end{cases} \quad (2)$$

where L_B is the present blade grid position, L_T the present transition grid position; T_B is a transformation matrix and consists of four subsequent motions: $R_{\theta(t)}$ (feathering motions), $R_{\beta(t)}$ (flapping motions), $R_{\psi(t)}$ (rotation motions), and $R_{\phi(t)}$ (tilting and translational motions); T_T is a transformation matrix that contains tilting and translational motions, the subscript "0" represents the previous position.

2.2. Rotor actuator disk

In the VBM, a moving-embedded grid system (see Fig. 1) around the rotor modeled as an actuator disk is established. For the actuator disk model in this paper, the rotor is described as a grid surface, and the distribution of grid points in the disk is not restricted to account for actual blade motions.

2.3. Real blade grid

In the RBM, a new multi-layer moving-embedded grid system which consists of C–O type body-fitted grids (see Fig. 2) around the blade, regular transition grids, and background grids is established. To reduce the dissipation of the rotor wake effectively, the transition grids embedded in the background grid system are employed to describe the relative motions of
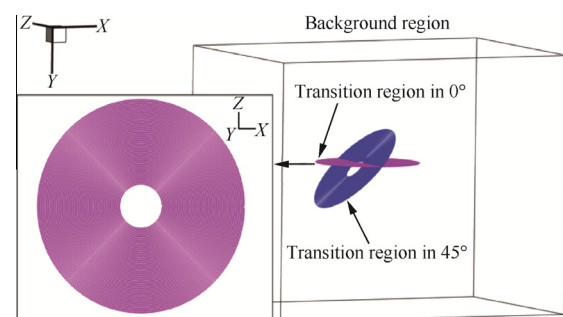

Fig. 1 Schematic of actuator disk instead of rotor in the grid system.

the blades, which include rotating, cyclic pitching, cyclic flapping, tilting, and transiting motions. Considering the unsteady variation of the rotor flowfield in a conversion mode, the grids in the transition zone are refined to ensure the solution accuracy. Therefore, during a conversion mode of the tilt-rotor, the background grids must be distributed uniformly in three dimensions to maintain the interpolation precision between the transition grids and the background grids (see Fig. 3).

2.4. Embedded grid system

Preprocessing of the embedded grid (see Figs. 4 and 5) usually involves two steps: (A) identifying the hole boundary and hole points and (B) searching for suitable donor elements. A new searching algorithm, called adaptive inverse map (AIM), is proposed in the current investigation, which consists of the following three steps.

Step 1 Generate the inverse map (denoted by INMAP) over the objective grid O and adaptively adjust it to keep the relative position among the actual grids, in order to search for a suitable donor element bounding any point G efficiently, and the unit size of the INMAP in three dimensions should meet one of the three conditions in the following formulas:

$$\begin{cases} \Delta INMAP_x \approx \Delta x \\ \Delta INMAP_y \approx \Delta y \\ \Delta INMAP_z \approx \Delta z \end{cases} \tag{3}$$

where $\Delta INMAP_x$, $\Delta INMAP_y$, and $\Delta INMAP_z$ represent the unit size of the INMAP along x, y, and z directions, respectively, and Δx, Δy, and Δz represent the unit size of the object grid. Then identify the grid element in O that bounds any point of the INMAP, and predict the reference position of the point in the objective element. After that, only the indexes of the grids are stored in the INMAP

Step 2 Identify the donor element in the INMAP that bounds point G, and predict the reference position of the point in O.

Step 3 Obtain the interpolated data for the eight vertices of the donor element bounding point G from the known points, and subsequently get the information for point G by the trilinear interpolation method.
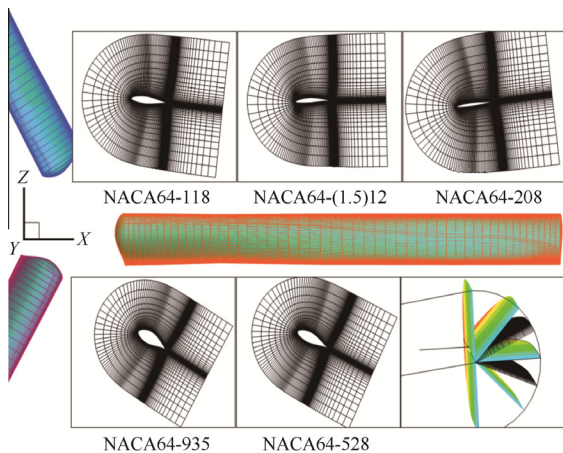

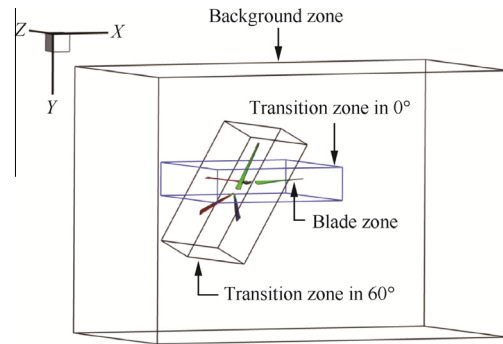**Fig. 2**   Schematic of the blade surface grid.

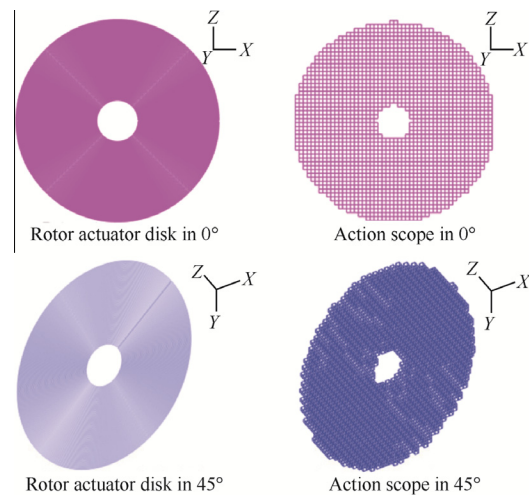**Fig. 3**   Schematic of the grid system in the RBM.

Fig. 4   Schematic of embedded grid system by the VBM.
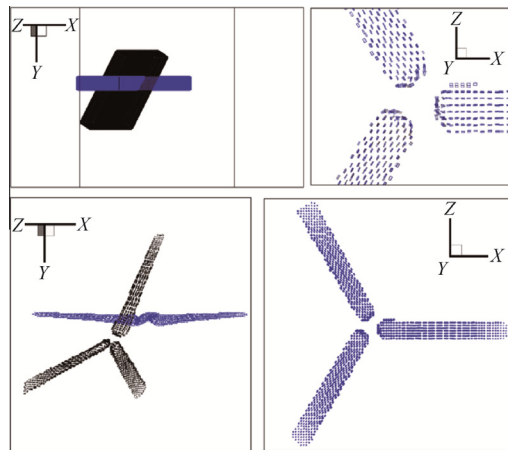

Fig. 5   Schematic of embedded grid system by the RBM.

In the searching process, only one block of the three-dimensional inverse map over the structured C–O grids around the rigid blade is needed, and the generated inverse map is used to get the interpolated data for the hole of the background grids from the objective grids. In addition, the identification of the corresponding donor elements for the outer boundary of the objective zone can be analytically performed. The analytical formulas are given as follows:

$$\begin{cases} \mathrm{II} = C_x(x,y,z), \mathrm{JJ} = C_y(x,y,z), \mathrm{KK} = C_z(x,y,z) \\ I_{\min} = \mathrm{INMAP}(1, \mathrm{II}, \mathrm{JJ}, \mathrm{KK}) \\ I_{\max} = \mathrm{INMAP}(2, \mathrm{II}, \mathrm{JJ}, \mathrm{KK}) \\ J_{\min} = \mathrm{INMAP}(3, \mathrm{II}, \mathrm{JJ}, \mathrm{KK}) \\ J_{\max} = \mathrm{INMAP}(4, \mathrm{II}, \mathrm{JJ}, \mathrm{KK}) \\ K_{\min} = \mathrm{INMAP}(5, \mathrm{II}, \mathrm{JJ}, \mathrm{KK}) \\ K_{\max} = \mathrm{INMAP}(6, \mathrm{II}, \mathrm{JJ}, \mathrm{KK}) \\ (I, J, K) = \mathrm{SEEK}(I_{\min}, I_{\max}, J_{\min}, J_{\max}, K_{\min}, K_{\max}) \end{cases} \quad (4)$$

where (II, JJ, KK) represent the indexes of the suitable elements in the INMAP; C_x, C_y, and C_z represent the relationship between the background coordinate and the INMAP; SEEK represents the relationship between the objective grid and the INMAP; (I, J, K) represent the indexes of the suitable donor elements.

3. Numerical methods

3.1. Governing equations

Based on the Cartesian coordinates, the 3-D compressible Navier–Stokes equations are used to solve the unsteady flowfield of the tilt-rotor. In this inertial frame, the system of equations is formulated in the terms of absolute velocities which are an important condition for accurate treatment of the numerical flux and the far-field boundary conditions. The equations are written in a finite volume form as

$$\frac{\partial}{\partial t} \int_V \boldsymbol{W} \mathrm{d}V + \oint_{\partial V} (\boldsymbol{F}_{\mathrm{c}} - \boldsymbol{F}_{\mathrm{v}}) \cdot \boldsymbol{n} \mathrm{d}s = s \int_V \boldsymbol{J} \mathrm{d}V \quad (5)$$

where $\boldsymbol{W}$ denotes the vector of conservative variables, $\boldsymbol{F}_{\mathrm{c}}$ the inviscid flux, $\boldsymbol{F}_{\mathrm{v}}$ the viscous flux, $\boldsymbol{J}$ represents the source term, $\boldsymbol{n}$ is the unit normal vector to the surface, V the volume of the grid cell, ∂V is the area of the grid cell, $s = \begin{cases} 1 & \mathrm{VBM} \\ 0 & \mathrm{RBM} \end{cases}$.

Jameson's second-order cell-centered finite volume approach with artificial viscosity is used in spatial discretization. For any grid unit, Eq. (5) is written as

$$V_{ijk} \frac{\mathrm{d}}{\mathrm{d}t} \boldsymbol{W}_{ijk} + \boldsymbol{F}_{cijk} - \boldsymbol{F}_{vijk} - \boldsymbol{J}_{ijk} = \boldsymbol{0} \quad (6)$$

where i, j, k is the grid indices.

One equation Spalart–Allmaras (S–A) turbulence model is taken to simulate the viscous effect. The S–A model can be written as

$$\frac{\partial \tilde{v}}{\partial t} + U_j \frac{\partial \tilde{v}}{\partial x_j} = c_{b1}(1 - f_{t2})\widetilde{S}\tilde{v} - \left(c_{w1} f_w - \frac{c_{b1}}{k^2} f_{t2}\right)\left(\frac{\tilde{v}}{d}\right)^2$$
$$+ \frac{1}{\sigma} \cdot \frac{\partial}{\partial x_k}\left[(v + \tilde{v})\frac{\partial \tilde{v}}{\partial x_k}\right] + \frac{c_{b2}}{\sigma} \cdot \frac{\partial \tilde{v}}{\partial x_k} \cdot \frac{\partial \tilde{v}}{\partial x_k} \quad (7)$$

where c_{b1}, c_{w1}, c_{b2}, k and σ are constants, f_{t2} and f_w represent the procedure variable, $\widetilde{S}$ stands for the modified magnitude of the mean rotation rate, v denotes the laminar kinematic viscosity, d is the distance to the closest wall, $\tilde{v}$ the modified eddy viscosity, and U is the velocity. The terms on the left side of the equation are the unsteady and convection terms, and the terms on the right side are the production, destruction, dissipation, and diffusion terms, respectively.

3.2. Time discretization

A dual time-stepping approach is adopted in the current investigation for predicting the unsteady three-dimensional flowfield of the tilt-rotor under a conversion condition. In this approach, the solution is marched forward in pseudo-time to a steady state through an implicit LU-SGS scheme at each physical time level. During the marching in pseudo-time, the physical time is fixed, which permits the acceleration techniques of steady flow calculations such as a local time-stepping scheme to be used. Therefore, Eq. (6) can be replaced by

$$V \frac{\partial \boldsymbol{W}_{ijk}}{\partial t} + V \frac{3\boldsymbol{W}_{ijk}^{n+1} - 4\boldsymbol{W}_{ijk}^n + \boldsymbol{W}^{n-1}}{2\Delta t} + \mathbf{Res}(\boldsymbol{W}^{n+1}) = 0 \quad (8)$$

where n stands for the present time level.

The residual value **Res** is to be line processed as

$$\left[\left(\frac{V}{\Delta\tau} + \frac{3V}{2\Delta t}\right)I + \frac{\partial \boldsymbol{R}}{\partial \boldsymbol{W}_{ijk}}\right]\Delta\boldsymbol{W}_{ijk}$$
$$= -\frac{3\boldsymbol{W}_{ijk}^{n+1} - 4\boldsymbol{W}_{ijk}^n + \boldsymbol{W}^{n-1}}{2\Delta t} - \mathbf{Res}^m \quad (9)$$

where Δt is the physical azimuthal step: $\Delta t = 2\pi/\Omega_{\mathrm{tilt}} \mathrm{IB}$, where IB is the number of computational interval angles along the tilting direction in the VBM, while $\Delta t = 2\pi/\Omega \mathrm{IB}$, where IB is the number of computational azimuthal angles along the circumferential direction in the RBM. The pseudo-time step $\Delta\tau$ is restricted by stability considerations. For each cell, the allowable pseudo-time step is chosen as

$$\Delta\tau_{i,j,k} = \min\left(\frac{2}{3}\Delta t, \frac{\mathrm{CFL}V_{i,j,k}}{\lambda_{\mathrm{c},i} + \lambda_{\mathrm{c},j} + \lambda_{\mathrm{c},k} + 2(\lambda_{\mathrm{v},i} + \lambda_{\mathrm{v},j} + \lambda_{\mathrm{v},k})}\right) \quad (10)$$

where $\lambda_{\mathrm{c},i}$, $\lambda_{\mathrm{c},j}$, and $\lambda_{\mathrm{c},k}$ are the spectral radii of the Jacobian matrices of flux vectors in the i, j, and k directions, $\lambda_{\mathrm{v},i}$, $\lambda_{\mathrm{v},j}$, and $\lambda_{\mathrm{v},k}$ are the viscous spectral radii in the i, j, and k directions, respectively, and CFL represents the Courant number.

The LU-SGS scheme is used to solve Eq. (9) as

$$(\boldsymbol{L}_n + \boldsymbol{D}_n)\boldsymbol{D}_n^{-1}(\boldsymbol{D}_n + \boldsymbol{U}_n)\Delta\boldsymbol{W}_{ijk} = -\frac{3\boldsymbol{W}_{ijk}^n - 4\boldsymbol{W}_{ijk}^{n-1} + \boldsymbol{W}^{n-2}}{2\Delta t} - \mathbf{Res}^n \quad (11)$$

where $\boldsymbol{L}_n$ is the lower triangular matrix, $\boldsymbol{U}_n$ the upper triangular matrix, $\boldsymbol{D}_n$ the diagonal matrix.

The system matrix of the LU-SGS scheme (Eq. (11)) can be inverted in three steps.

(1) Forward sweep
$$(\boldsymbol{L}_n + \boldsymbol{D}_n)\Delta\boldsymbol{W}_{ijk} = -\mathbf{Res}^n \quad (12)$$

(2) Backward sweep
$$(\boldsymbol{D}_n + \boldsymbol{U}_n)\Delta\boldsymbol{W}_{ijk}^n = \boldsymbol{D}_n\Delta\boldsymbol{W}_{ijk} \quad (13)$$

(3) Update
$$\boldsymbol{W}_{ijk}^{n+1} = \boldsymbol{W}_{ijk}^n + \Delta\boldsymbol{W}_{ijk}^n \quad (14)$$

3.3. Virtual blade model

The simulation of the tilt-rotor can be simplified by modeling the rotor as an infinite thin disk called "actuator disk".[19,20] It represents that the loads of the rotor are averaged in time and
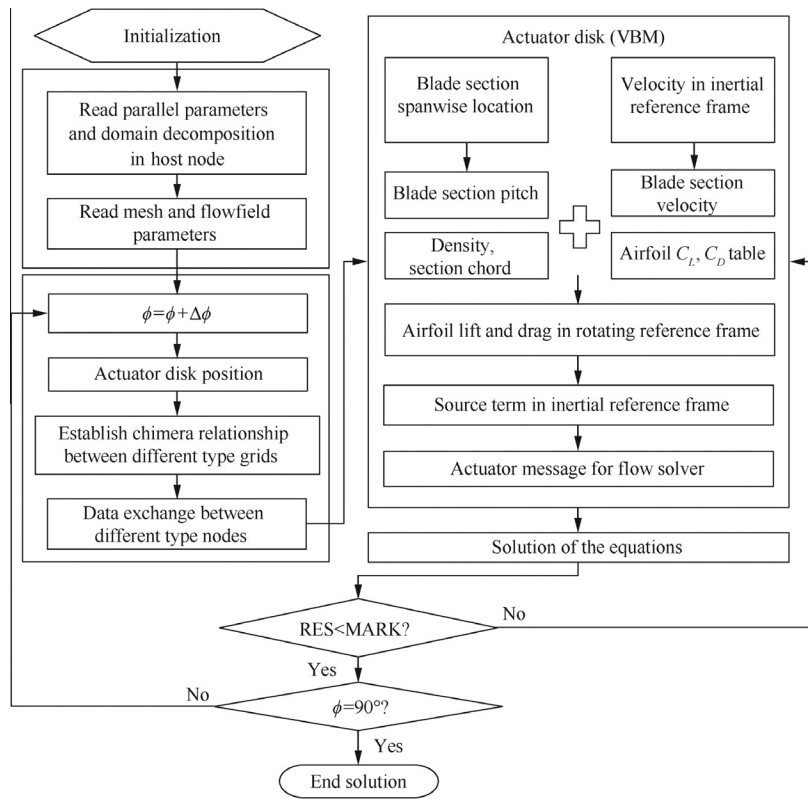
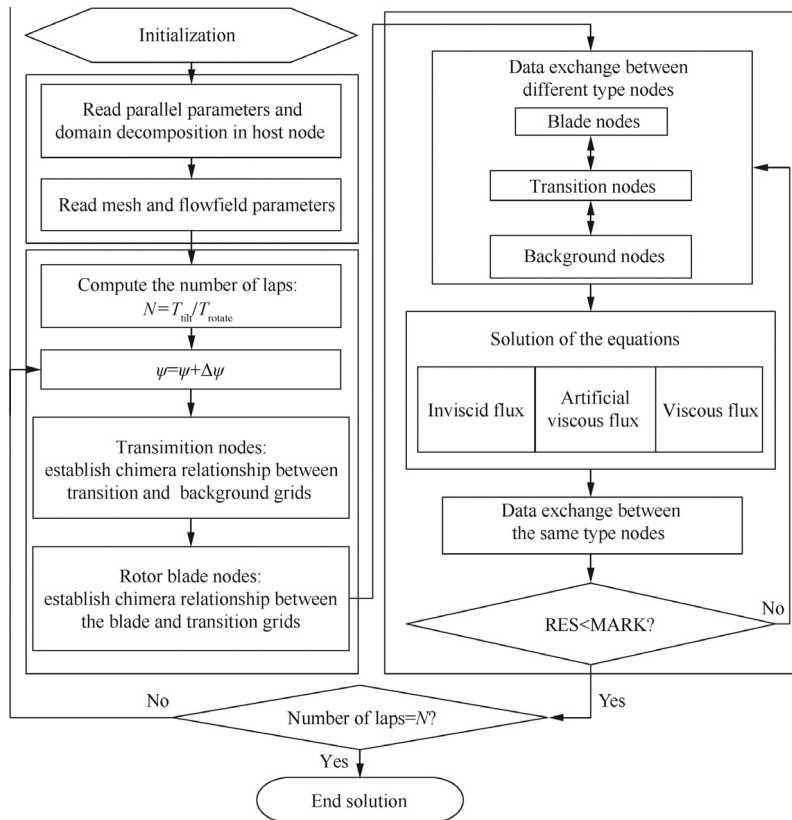**Fig. 6**   Flowchart about the momentum source calculation in the VBM method.

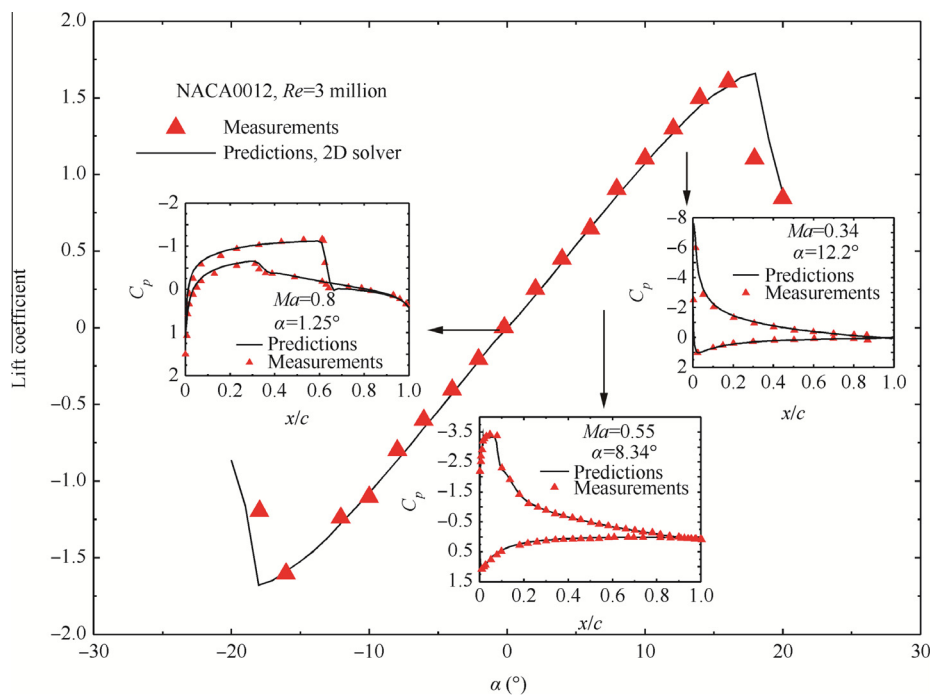**Fig. 7**   Schematic of the RBM simulation processes.

Fig. 8 Comparisons of predicted lift coefficient distributions of the NACA0012 airfoil with experimental data.
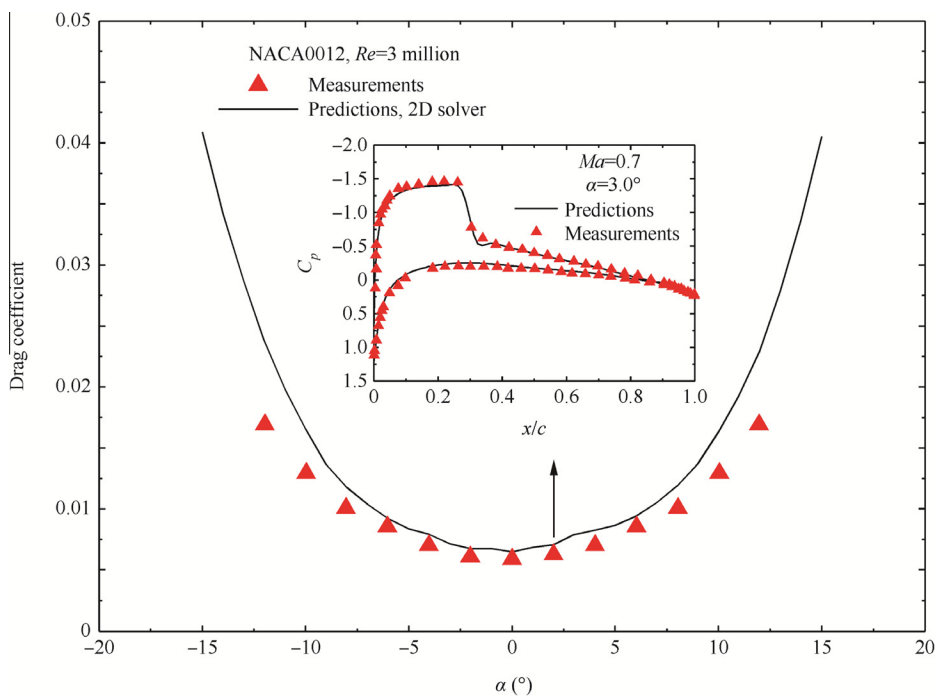

Fig. 9 Comparisons of predicted drag coefficient distributions of the NACA0012 airfoil with experimental data.

applied to a grid surface in a steady flow computation. According to the steady-state assumption, a distinct reduction of computational cost is achieved compared to an unsteady calculated result of the flow around rotating blades.

The actuator disk model is introduced into the code as a particular boundary condition where discontinuous aerodynamic quantities are prescribed (in Eq. (5)), and two parts need

to be considered when determining the influence of the tilt-rotor on its flowfield. One part is to find the locations in the physical or computational domain where the influence is felt (see Fig. 4). The other is to determine the momentum source terms J in Eq. (5) which behave as a normal interface, and the actuator disk source terms are simply added to residuals at these locations.

Table 1 Two-bladed typical rotor parameters.

Parameter	Metric
Airfoil section	NACA0012
Rotor radius (m)	0.914
Blade chord (m)	0.1
Tip Mach number	0.3285
Collective pitch angle $\varphi_0(°)$	11
Blade twist (°)	0

At first, a tiny element whose area is S_Δ on the plane of the actuator disk is investigated, which is located at a distance of r from the center of the tilt-rotor hub with a length of dr along the spanwise direction and a width of $\Delta\psi$ along the circumferential direction. Suppose that the instantaneous force acting on the blade is dF, and the reacting force acting on the fluid element at this location is $-dF$ and the resultant force is $-NdF$ for N blades. As a result, the time averaged force acting on the surface of the grid cell is

$$F_\Delta = -\frac{NdF}{2\pi rdr}S_\Delta \qquad (15)$$

Then, dF in the tiny element can be calculated. For a rotor reference frame, the forces can be written as

$$\begin{cases} \beta_* = \arctan\frac{V_Z}{V_O}, \\ \alpha = \varphi - \beta_* \\ dT = dL\cos\beta_* - dD\sin\beta_* \\ dQ = -dL\sin\beta_* - dD\cos\beta_* \\ dF = -dT - dQ \end{cases} \qquad (16)$$

(a) Y=0.215R

(b) Y=0.325R
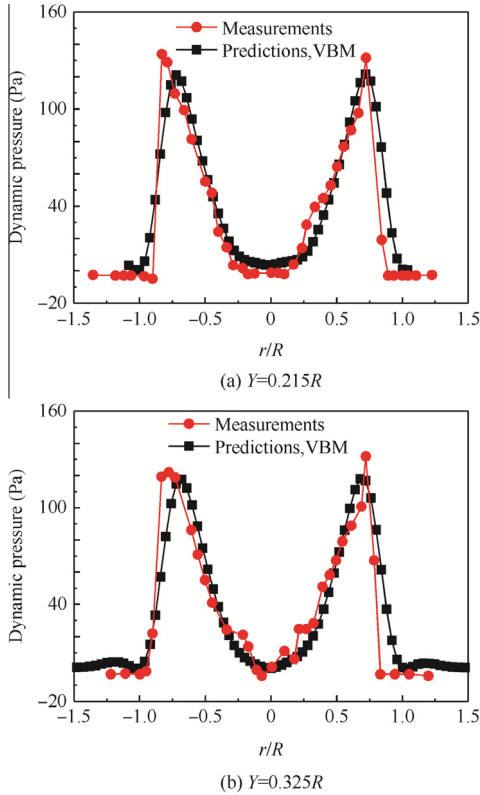
Fig. 10 Comparisons of predicted dynamic pressure distributions with experimental data.

where α is the effective angle of attack, φ the local collective angle, β_* the angle of incidence, V_Z the relative axial velocity, V_O the relative tangential velocity, dL the lift of the airfoil, dD the drag of the airfoil, and lift coefficient C_L and drag coefficient C_D can be obtained by a 2D-Reynolds averaged Navier–Stokes solver. Fig. 6 shows the flowchart about the momentum source calculation in the VBM method.

3.4. Real blade model

In current investigation, the whole flowfield is divided into three zones which are shown in Fig. 3. The first zone covers a small region around each blade. In this zone, the viscous effect is modeled using a Navier–Stokes solver. The second zone covers the first zone to reduce the dissipation of the wake due to truncation errors and artificial viscosity presented in numerical algorithms. The third zone includes the inviscid region away from the blade, which is usually located one or more rotor diameters away from the rotor disk. The latter two zones are modeled by using an Euler solver. To allow the vortex to propagate out from the Navier–Stokes zone to the inviscid zone without false reflections, the embedded region between the three zones need be carefully handled.

In order to improve the computational efficiency, the single program multiple data (SPMD) model parallel acceleration technology[21] has been adopted. Careful consideration of parallel computing issues including load balancing and re-establishing data communication becomes critical to ensure efficient computational performance. Spatial decomposition for parallel processing is achieved by distributing grids among the processors. The grid size in this investigation is over 3.7 million elements. Taking a revolution with 10800 iterations as an example, only 3.2 h are consumed by using 5 processors in the simulations compared to 13.4 h by a single CPU. The results indicate 4.2 time acceleration compared to the single CPU implementation, and the acceleration efficiency is over 80%. The numerical example shows that the parallel method can achieve a better parallel speedup ratio and also save the storage efficiently. Fig. 7 illustrates the whole RBM processes in a simplified sequence flow diagram.

4. Results and discussions

The two analytical methods proposed in this work are validated by comparing the calculated results of an NACA0012 airfoil under different working conditions, a two-bladed typical rotor, and a three-bladed tilt-rotor in hover with available experimental data. In addition, full and fixed conversion cases are calculated by the VBM or RBM respectively in order to investigate the unsteady aerodynamic characteristics of the tilt-rotor.

Table 2 Three-bladed Branum–Tung tilt-rotor parameters.

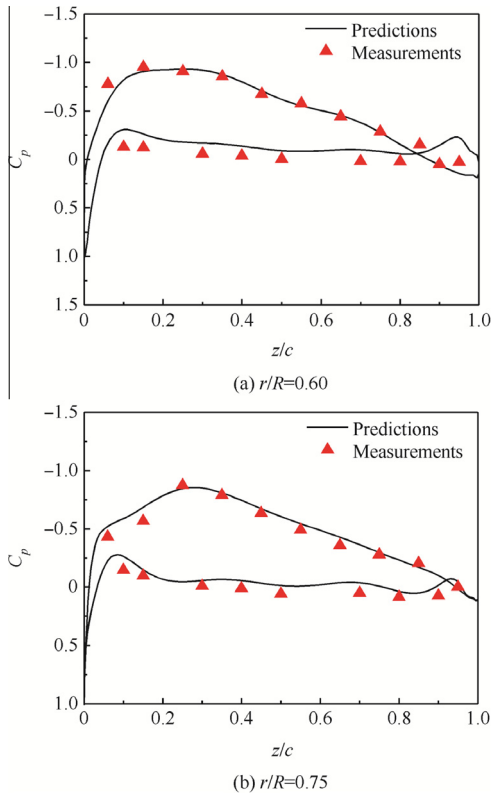| Parameter	Metric
Airfoil section	NACA64 series
Rotor radius (m)	0.61
Rotor solidity	0.1194
Tip Mach number	0.338
Collective pitch angle (°)	8
Blade twist (°)	−32

(a) r/R=0.60

(b) r/R=0.75

Fig. 11 Comparisons of pressure coefficient distributions of the Branum–Tung blade in hover with experimental data.

4.1. 2D airfoil case

Simulations for the flowfield of the NACA0012 airfoil are conducted by the present method (simplified from a 3D RBM solver), and the size of the C-type grid around the airfoil is 193×49. Fig. 8 shows the lift coefficient C_L distributions along the angle of attack and the airfoil surface pressure coefficient C_p distributions at three different positions, and Fig. 9 shows the drag coefficient C_D distributions along the angle of attack and the surface pressure coefficient distribution at a fixed position. It is clearly seen from the comparisons in the figures that the results predicted by using the proposed 2D solver agree well with the experimental data.
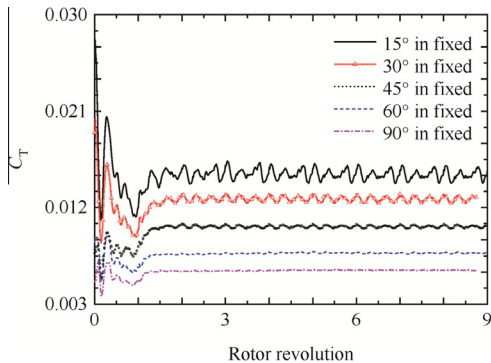
4.2. Two-bladed typical rotor

The parameters of the typical rotor[22] are given in Table 1. The VBM is validated in this numerical case, and the size of the background grids is $117 \times 121 \times 85$. Fig. 10 shows comparisons between predicted dynamic pressure distributions (r/R is the proportional position of the span direction) and experimental data at different axial positions below the rotor disk, which demonstrate good agreements between the calculated results and experimental data. It shows that the proposed VBM method is effective to simulate the flowfield of the rotor.

4.3. Three-bladed Branum–Tung tilt-rotor

A tilt-rotor with three blades[23] is taken as the numerical example to verify the effectiveness of the RBM, the size of the C–O type blade grids of which is $193 \times 49 \times 65$ and the size of the background grids is $117 \times 121 \times 85$. The rotor parameters or characteristics are given in Table 2. Fig. 11 compares the calculated pressure coefficients of the blade section along the spanwise of the blade with the experimental results, and they agree well with each other, which indicates that the RBM method is capable to capture the flowfield around the tilt-rotor blades in a hover mode.

4.4. Tilt-rotor in a conversion mode

A whole XV-15 tilt-rotor conversion case from 0° (vertical) to 90° (horizontal) is used to analyze the aerodynamic effects of unsteady movement of the tilt-rotor and the difference between the whole and fixed conversion modes. In this case, the size of the C-O type blade grids is $193 \times 49 \times 65$, the size of the transition grids is $125 \times 61 \times 125$, and the size of the background grids is $117 \times 121 \times 85$. The operating conditions of the rotor are: advance ratio $\mu = 0.15$, tip Mach number $Ma_{tip} = 0.69$, $\theta_0 = 15°$, and conversion time $T_{tilt} = 5$ s.

Because of the differences in flow conditions, the simulation process of XV-15 in a fixed conversion mode requires about three rotor revolutions for the force history to fully converge to the periodic state in the RBM, as illustrated in Fig. 12, where C_T is thrust coefficient. Fig. 13 gives the calculated thrust coefficient distributions of a blade in a conversion mode by the RBM. As clearly demonstrated in the results, the thrust decreases gradually and smoothly with the increase of the tilt
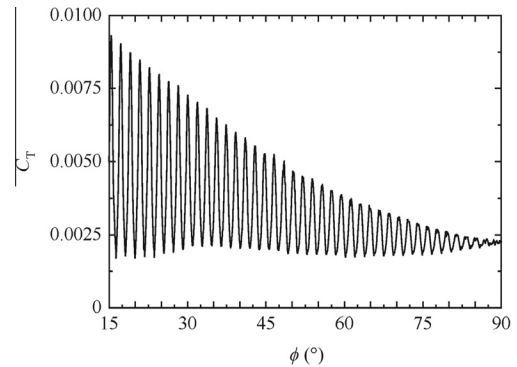

Fig. 12 Convergence history of thrust coefficient of the XV-15 tilt-rotor in a fixed conversion mode.

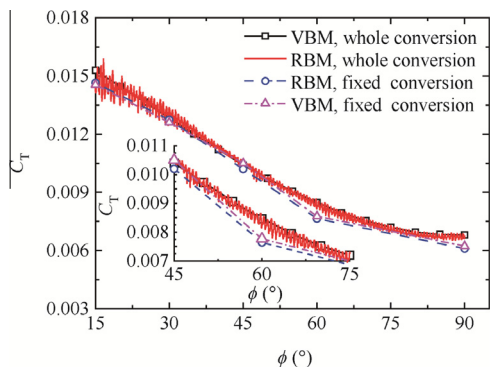**Fig. 13** Thrust coefficient distributions of the XV-15 blade in a conversion mode.

Fig. 14 Thrust coefficient distributions of the XV-15 tilt-rotor in different conversion modes.

Table 3 Comparisons of CPU time between the two solvers.

Calculation case	Cost time (h)	
	VBM	RBM
A fixed conversion case	0.29	9.57
A whole conversion case	26.1	153.7

angle. This phenomenon is caused by the decrease of the effective angle of attack due to the increase of the inflow angle.

Fig. 14 shows the thrust coefficient distributions of the tilt-rotor in different conversion modes calculated by the VBM and RBM methods respectively. The thrust variations of the tilt-rotor calculated from the VBM and the RBM show a similar behavior. By the comparisons of the lift coefficient variations, it can be seen that good agreements between the calculated results by the VBM and the RBM are observed in different conversion modes. There is basically a slight increase of the tilt-rotor lift coefficient in the whole conversion mode compared to the fixed conversion mode, due to the impact of the tilting motion in the whole conversion mode, which is beneficial for keeping the produced lift of the tilt-rotor in an actual conversion mode.

In the present investigation, the developed codes are set up on a cluster with 14 I7 (3.4 G) CPUs. The computational resource requirements are compared between the VBM and the stand-alone RBM in a conversion mode. The comparisons are given in Table 3, and the simulations by the two methods are performed in the same background grids.

For the VBM calculation in a fixed conversion mode, the converged solution can be achieved in approximately 0.29 h on 5 processors. For the same case considered, the computation time is about 9.57 h by using the proposed RBM method. A typical calculation for the whole conversion mode condition requires approximately 154 h of CPU time, which needs about 50 rotor revolutions and 50 iterations for a step size of 5° in the azimuthal position to obtain a converged solution by the RBM calculations. It is demonstrated that from the point of computational efficiency, it would be better to use the VBM method to analyze the overall performance of the tilt-rotor in the whole conversion, instead of the RBM method.

Fig. 15 gives the calculated thrust coefficient Ma^2C_n (C_n is the normal force coefficient) distributions along the blade

(a) $\phi=15°$

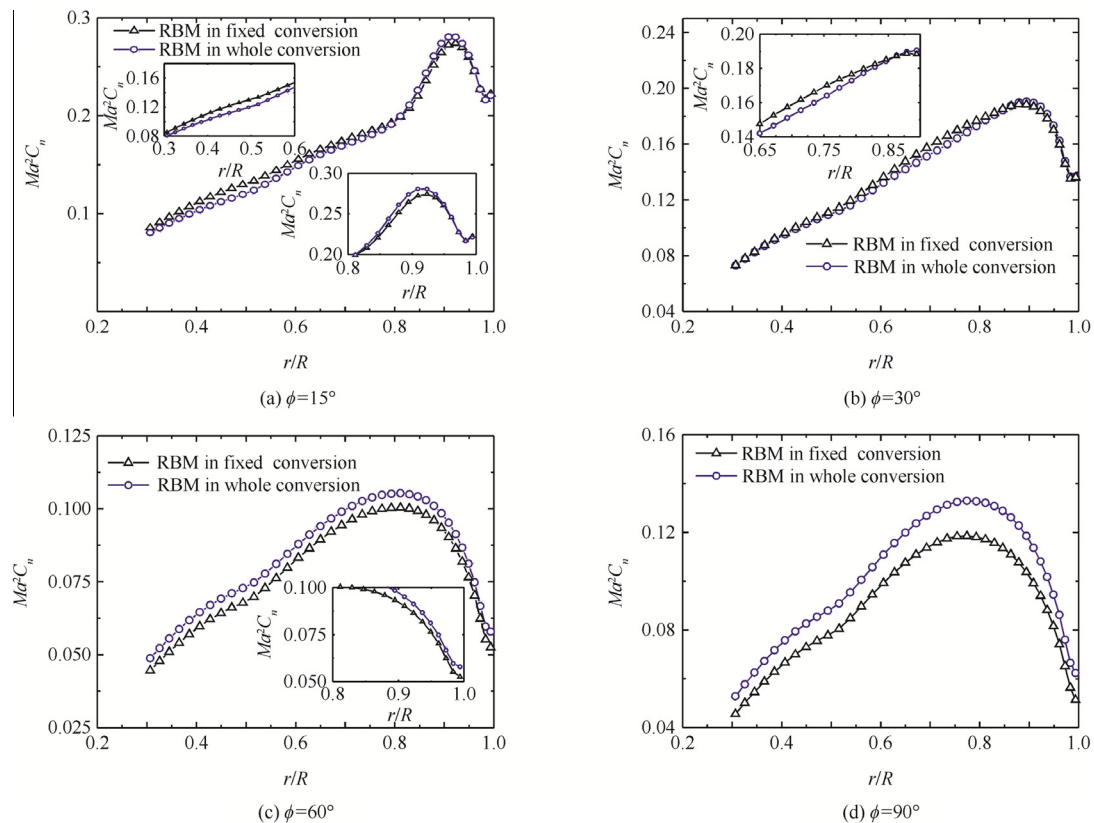(b) $\phi=30°$

(c) $\phi=60°$

(d) $\phi=90°$

Fig. 15 Comparisons of local thrust coefficient distributions along the XV-15 blade spanwise on the advancing side between the whole and fixed conversion modes.
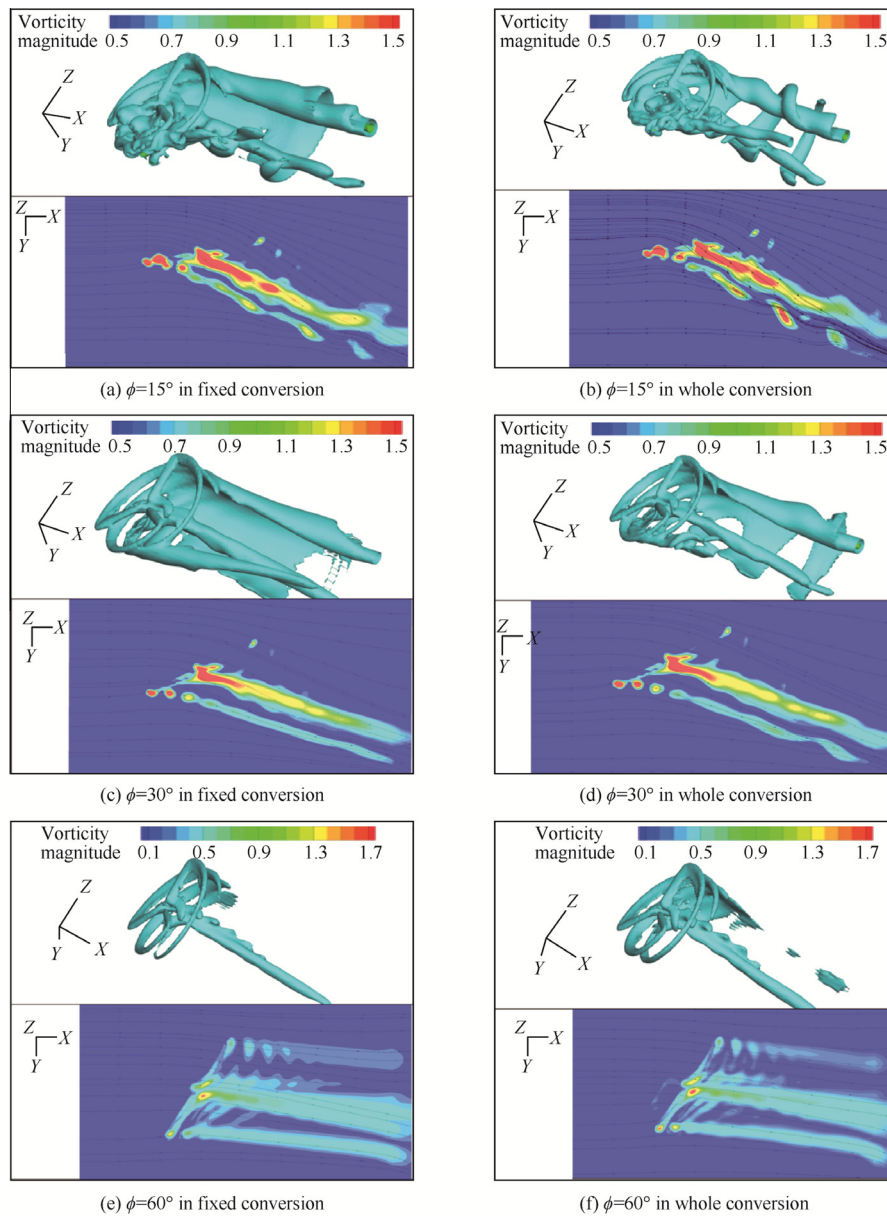
Fig. 16 Comparisons of vorticity magnitude and iso-vorticity contour in whole and fixed conversion flights (in the background grid).
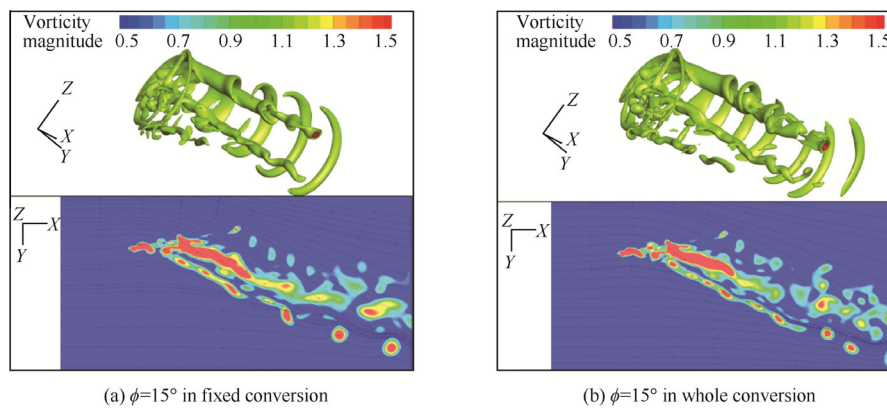

Fig. 17 Comparisons of vorticity magnitude and iso-vorticity contour in whole and fixed conversion flights by the refined grid (in the background grid).

(a) ϕ=15° in fixed conversion

(b) ϕ=30° in fixed conversion

(c) ϕ=45° in fixed conversion

(d) ϕ=60° in fixed conversion
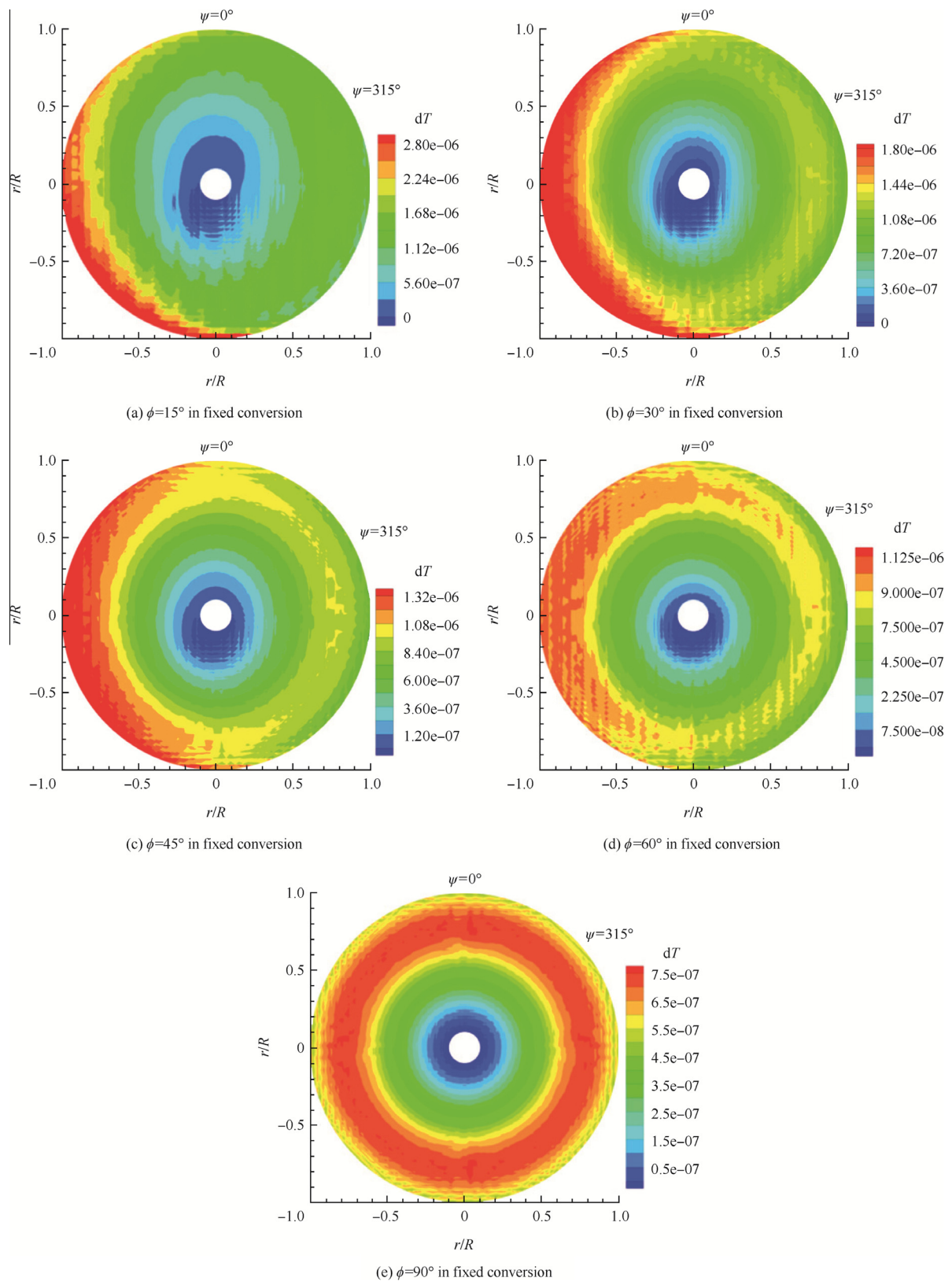
(e) ϕ=90° in fixed conversion

Fig. 18   Predicted normalization rotor thrust distributions in the fixed conversion mode.

spanwise at the advancing side in four different conversion modes at 15°, 30°, 60°, and 90° tilt angles by using the RBM. Different calculated results show that majority of thrust is generated outboard on the blade, and similar distributions along the blade are calculated by the RBM method. However, it can be clearly seen that thrust has a slightly smaller value in

the whole conversion than the fixed conversion at 15°, while a reverse trend is shown in the rest majority of tilt angles. These differences are caused by effectively capturing the unsteady aerodynamic characteristics of the tilt-rotor in the whole conversion mode by the RBM.

To illustrate the aerodynamic interference of the tilt-rotor in the whole conversion mode, different flowfields of the XV-15 tilt-rotor at three typical tilt angles in a conversion mode are shown in Fig. 16. The flowfield around the tilt-rotor blade is captured well, which indicates the good potential of the present method in calculating the unsteady aerodynamic force of the rotor in a conversion mode. A stronger and distorted blade-tip wake in the whole conversion mode is obviously observed than that of the fixed conversion mode. As the increase of the tilt angle, this phenomenon is gradually weakened, and the main reason is due to the increase of the inflow speed.

In order to capture the unsteady flowfield of the tilt-rotor more accurately at the conversion regions where the unsteady flow characteristics change rapidly, more grid points should be generated in the calculations. Fig. 17 gives the comparisons of the different flowfields calculated by the two methods using the same refined background grids ($233 \times 193 \times 169$). A more obvious wake distortion in the whole conversion mode can be observed compared with that in the fixed mode calculated by the RBM. It can also be seen from the figures that the vortex shed from the tilt-rotor is captured more clearly than that shown in Fig. 16 at the same condition.

Fig. 18 shows the rotor thrust variations of the tilt-rotor over the whole rotor disk at different tilt angles. For the two conversion states of tilt angles $\phi = 15°$ and $\phi = 30°$, it is found that the maximum thrust is located between 90° and 270° azimuthal angles. However, the amplitudes decrease with the increase of the tilt angle, as shown in Fig. 16. It indicates that the free stream decreases the blade's effective angle of attack, resulting in the special rotor loading distribution in this region. With the increase of the tilt angle, thrust distributions of the tilt-rotor become gradually uniform over the whole azimuth and the thrust of the blade root increases gradually.

5. Conclusions

VBM/RBM solvers are developed in this work to predict the flowfield around a tilt-rotor in a conversion mode. The developed solvers are validated through comparing the calculated results with the available experimental data. The solvers are also used to investigate the effects of different flight modes on the tilt-rotor flowfield.

(1) A combination of the moving-embedded grid methodology and the AIM methodology can account for the rigid blade motions in a conversion mode, and is shown to be effective and robust in searching for the corresponding donor elements and getting the interpolated data for the information communication among different calculation zones. The proposed multi-layer moving-embedded grid technique is capable of capturing effectively the unsteady characteristics of the flowfield of the tilt-rotor in a conversion mode.

(2) The proposed VBM and RBM are proved to be effective in predicting the complicated three-dimensional unsteady flowfield of the tilt-rotor in a conversion mode

with a dual-time method. The established RBM can provide a more detailed flowfield of the tilt-rotor in a conversion mode than the VBM. Compared with the RBM, the VBM results are consistent with the RBM results in analyzing the overall aerodynamic performance of the tilt-rotor in the whole conversion mode. From the point of computational efficiency, the VBM shows as a more attractive choice to investigate the whole conversion mode. Meanwhile, it is evident that the SPMD model parallel acceleration technology adopted in the two methods significantly increases the computation efficiency.

(3) Due to the impact of the tilting motion in the whole conversion mode, the values of unsteady aerodynamic forces in the whole conversion mode are basically larger than those in the fixed conversion mode, and a stronger and distorted blade-tip wake in the whole conversion mode is formed compared to the fixed conversion mode. All the unsteady aerodynamic phenomena diminish gradually with the increase of the tilt-angle.

References

1. Maisel MD, Giulianetti DJ, Dugan DC. The history of the XV-15 rotor research aircraft: from concept to flight. Washington, D.C.: NASA; 2000 Jan. Report No.: NASA SP-2000-4517.
2. Johnson W, Yamauchi GK, Watts ME. Designs and technology requirements for civil heavy lift rotorcraft. *AHS vertical lift aircraft design conference*. Alexandria: AHS International; 2006.
3. Yeo H, Johnson W. Performance and design investigation of heavy lift tilt-rotor with aerodynamic interference effects. *J Aircr* 2009;**46**(4):1231–9.
4. Felker FF, Maisel MD, Betzina MD. Full-scale tilt-rotor hover performance. *J Am Helicopter Soc* 1986;**31**(2):10–8.
5. Yamauchi GK, Wadcock AJ, Heineck JT. Surface flow visualization on a hovering tilt rotor blade. *An American Helicopter Society technical specialists' meeting for rotorcraft acoustics and aerodynamics, VA*. Alexandria: AHS International; 1997.
6. Lau BH, Wadcock AJ, Heineck JT. Wake visualization of a full-scale tilt rotor in hover. *An American Helicopter Society technical specialists' meeting for rotorcraft acoustics and aerodynamics, VA*. Alexandria: AHS International; 1997.
7. Wadcock AJ, Yamauchi GK, Driver DM. Skin friction measurements on a hovering full-scale tilt rotor. *J Am Helicopter Soc* 1999;**44**(4):312–9.
8. Radhakrishnan A, Schmitz FH. Quad tilt rotor download and power measurements in ground effect. *An 24th applied aerodynamics conference*. Alexandria: AHS International; 2006.
9. Li CH, Zhang J, Xu GH. Computational analysis on tiltrotor aerodynamic characteristics for transitional flight. *Acta Aerodynamica Sinica* 2009;**27**(2):173–9 [Chinese].
10. Poling DR, Rosenstein H, Rajagopalan G. Use a Navier-Stokes code in understanding tilt-rotor flowfields in hover. *J Am Helicopter Soc* 1998;**43**(2):103–9.
11. Gupta V, Baeder J. Investigation of quad tilt-rotor aerodynamics in forward flight using CFD. *An 20th AIAA Applied Aerodynamics Conference*. Reston: AIAA; 2002.

12. Potsdam MA, Strawn RC. CFD simulation of tiltrotor configurations in hover. *An American helicopter society 58th annual forum*. Alexandria: AHS International; 2002.

13. Lee-Rausch EM, Biedron RT. Simulation of an isolated tiltrotor in hover with an unstructured overset-grid RANS solver. *An American helicopter society 65th annual forum*. Alexandria: AHS International; 2009.

14. Wissink A, Potsdam M, Sankaran V. A coupled unstructured-adaptive Cartesian CFD approach for hover prediction. *An American Helicopter Society 66th annual forum*. Alexandria: AHS International; 2010.

15. Potsdam M, Strawn R. CFD simulations of tiltrotor configurations in hover. *J Am Helicopter Soc* 2005;**50**(1):82–94.

16. Sheng CH, Narramore JC. Computational simulation and analysis of Bell Boeing quad tilt-rotor aero interaction. *An American Helicopter Society 64th annual forum*. Alexandria: AHS International; 2008.

17. Zhao QJ, Xu GH, Zhao JG. Numerical simulations of the unsteady flowfield of helicopter rotors on moving embedded grids. *Aerosp Sci Technol* 2005;**9**(2):117–24.

18. Zhao QJ, Xu GH, Zhao JG. New hybrid method for predicting the flowfields of helicopter rotors. *J Aircr* 2006;**43**(2):132–40.

19. Ruith MR. Unstructured, multiplex rotor source model with thrust and moment trimming – Fluent's VBM model. *An 23rd AIAA applied aerodynamics conference*. Reston: AIAA; 2005.

20. Zhang Y, Ye L, Yang S. Numerical study on flow fields and aerodynamics of tilt rotor aircraft in conversion mode based on embedded grid and actuator model. *Chin J Aeronaut* 2015;**28**(1):93–102.

21. Allen CB. Parallel flow-solver and mesh motion scheme for forward flight rotor simulation. Reston: AIAA; 2006. Report No.: AIAA-2006-3476.

22. McKee JW, Naeseth RL. Experimental investigation of the drag of flat plates and cylinders in the slipstream of a hovering rotor. Washington, D.C.: Langley Aeronautical Laboratory; 1958 Apr. Report No.: NACA-TN-4239.

23. Branum L, Tung C. Performance and pressure data from a small model tiltrotor in hover. Washington, D.C.: AMES Research Center; 1997 Apr. Report No.: NASA TM 110441.

Li Peng is a Ph.D. student in aircraft design at Nanjing University of Aeronautics and Astronautics, and his research interests are helicopter CFD, parallel computation, and flight control on tilt-rotor aircraft.

Zhao Qijun is a professor and Ph.D. advisor in the College of Aerospace Engineering at Nanjing University of Aeronautics and Astronautics, where he received his Ph.D. degree in aircraft design. His main research interests are helicopter CFD, helicopter aerodynamics, aerodynamic shape design of rotor blades, active flow control on aerodynamic characteristics of rotors, and rotor aeroacoustics.

Zhu Qiuxian is an M.E. student in aircraft design at Nanjing University of Aeronautics and Astronautics, and her research interests are helicopter CFD, helicopter aerodynamics, and flight control on tilt-rotor aircraft.